Resonance-enhanced inelastic He-atom scattering from subsurface optical phonons of Bi(111)

Patrick Kraus,[1,2,*] Anton Tamtögl,[1] Michael Mayrhofer-Reinhartshuber,[1] Giorgio Benedek,[2,3] and Wolfgang E. Ernst[1]
[1]*Institute of Experimental Physics, Graz University of Technology, Graz, Austria*
[2]*Donostia International Physics Center (DIPC) and University of the Basque Country (EHU-UPV), Donostia/San Sebastián, Spain*
[3]*Dipartimento di Scienza dei Materiali, Università degli Studi di Milano-Bicocca, Milano, Italy*
(Received 18 April 2013; published 26 June 2013; corrected 28 June 2013)

Helium-atom scattering angular distributions from Bi(111) show a number of selective-adsorption resonance features corresponding to three bound states of the He atom in the surface-averaged Bi(111) potential. They are well represented by a 3-9 potential with a potential depth of 8.3 meV. The bound-state resonance enhancement of inelastic scattering is shown to provide the mechanism for the observation of subsurface optical phonons and for their comparatively large intensity.

DOI: 10.1103/PhysRevB.87.245433 PACS number(s): 34.35.+a, 68.49.Bc, 34.50.−s, 68.43.Mn

I. INTRODUCTION

It has been recently shown that inelastic helium-atom scattering (iHAS) from metal surfaces can detect subsurface phonons localized several layers beneath the surface, the depth being determined by the range of the electron-phonon (e-p) interaction.[1,2] This effect is particularly pronounced in ultrathin metallic films where the e-p interaction receives the largest contribution from quantum-well (QW) electronic bands and QW-confined phonons. A recent study by iHAS of the surface phonon dispersion curves in Bi(111) (Refs. 3–5) revealed unexpected large intensities from the optical branches of shear vertical (SV) polarization confined in the first bilayer (SV1 branch) as well as in the second bilayer (SV3 branch).

This can be better appreciated from a direct comparison of two iHAS spectra from the (111) surface of bismuth[4,5] and, e.g., six monolayers of lead on a Cu(111) substrate[6] measured under comparable kinematic conditions (Fig. 1). The optical surface phonons of Bi(111), which are separated from the acoustic band by a gap ranging 7.5–9.0 meV,[4,5] are considerably stiffer than the corresponding modes in the Pb(111) film (ϵ_1, ϵ_2) and would therefore be expected to have a weaker iHAS intensity. On the contrary, the iHAS intensity of the optical breathing mode (OBM) in the first bilayer (SV1) of Bi(111) is the largest of the spectrum [Fig. 1(a)], unlike that for the OBM (ϵ_1) in the first bilayer of Pb(111) which is weaker than the acoustic-mode intensities (α_1, α_2) [Fig. 1(b)]. On the other hand, the OBM in the second bilayer of Bi(111) (SV3) is much weaker than SV1, whereas in Pb(111) both the surface mode ϵ_1 and the subsurface mode ϵ_2 (localized at the Pb/Cu interface!) have comparable iHAS intensities, but are considerably weaker than the iHAS intensity from the acoustic branches α_1 and α_2.

One should now consider that for a conducting surface iHAS intensities are proportional to the square of phonon-induced surface charge density oscillations (SCDOs) and therefore to the corresponding mode-selected e-p coupling strengths.[1] A calculation based on density-functional perturbation theory (DFPT) for Bi(111) (Refs. 4 and 5) has shown that the SCDO induced by the breathing mode of the second bilayer (SV3) is about four times smaller than that for the first bilayer breathing mode (SV1) which means a factor 16 smaller iHAS intensity.

This is consistent with the fact that the surface conductivity of the Bi(111) surface is substantially restricted to the first bilayer, and accounts for the ratio SV3/SV1 of the optical-mode intensities as reported in Fig. 1(a). In our previous study[4,5] we found, however, that under certain kinematic conditions iHAS intensities from the optical SV3 modes were often comparable to those of SV1 optical modes, which allowed us to determine both branches with sufficient confidence. In a further analysis, reported in this work, we singled out a mechanism for the enhancement of iHAS intensities from subsurface optical modes which is specific to semimetal surfaces.

Despite the fact that semimetal surfaces are normally conducting and therefore possess free-surface electrons, they are found to be strongly corrugated, unlike the low-index surfaces of ordinary metals which are perfectly flat. This is due to the concentration of surface electrons and holes at the Fermi energy into comparatively narrow pockets around the symmetry points of the surface Brillouin zone (SBZ).[7] The surface corrugation, besides providing the intensities of elastic diffraction peaks and information on the surface geometry and the associated surface electron density, also allows for the selective adsorption of incident He atoms into surface bound states via the exchange of a reciprocal surface lattice vector. The interference between the direct and bound-state-mediated scattering channels yields a modulation of the elastic intensities and, more importantly in the present work, a modulation of the iHAS amplitudes (inelastic bound-state resonance). Actually a strong resonance enhancement can be obtained through a suitable tuning of the He beam incident angle and energy. This effect has been exploited in the past to detect high-energy optical surface phonons in insulators.[8,9]

In this paper we show that the comparatively strong iHAS amplitudes from the subsurface optical mode SV3 of Bi(111) are essentially due to a resonance enhancement involving the strongest bound-state resonance, $(1,0)_2$ with the $n = 2$ bound state and reciprocal-lattice vector $\mathbf{G} = (1,0)$. The possibility of tuning the curve representing the $(1,0)_2$ inelastic resonance condition in the energy-momentum space so as to make it nearly tangent to the optical SV3 dispersion curve allows us to measure it over a large portion of the SBZ. In this special kinematic situation, recently investigated and known as *surfing*,[10] the atom enters the bound-state channel inelastically by creating an optical SV3 phonon and rides for a while the

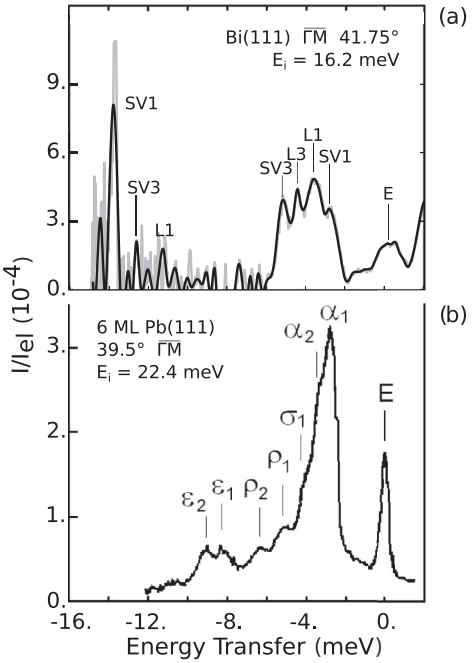

FIG. 1. Inelastic He atom scattering (iHAS) spectra from the (111) surface of (a) bismuth (Refs. 4 and 5) and (b) six monolayers of lead on a Cu(111) substrate (Ref. 6) measured under comparable kinematic conditions. The optical surface phonons of Bi(111) are separated from the acoustic band by a gap (7.5–9.0 meV) (Refs. 4 and 5) and are stiffer than the corresponding modes of the Pb(111) film (ϵ_1, ϵ_2). While in Bi(111) the iHAS intensity of the optical breathing mode (OBM) in the first bilayer (SV1) is much larger than that of the OBM in the second bilayer (SV3), in Pb(111) both surface (ϵ_1) and subsurface (ϵ_2 at the Pb/Cu interface) modes have comparable iHAS intensities, but are considerably weaker than the iHAS intensity from the acoustic branches α_1 and α_2. The grey line in (a) shows the actually measured signal while the black line is the result of averaging the original signal to constant energy bins.

running charge density wave associated with the SV3 mode, since both the trapped atom and the SV3 phonon travel at the same group velocity along the surface. This exotic form of atomic polaron allows for a strong coupling to the otherwise weak subsurface phonons.

The comparatively large diffraction amplitudes observed in both symmetry directions of Bi(111) reveal a fairly strong corrugation of the surface electron density, which reflects however the peculiar surface band structure better than the actual crystallography of the Bi atoms in the first bilayer. This is recognized from the equal depth of the two hollow sites of the surface unit cell, which would be inequivalent from the crystallographic point of view.[4,5] The bound-state energies derived from the selective adsorption angles have been obtained with sufficient precision to allow for a reliable prediction of the inelastic resonance conditions for the lowest bound states and the smallest G vectors.

Bismuth, besides being a semimetal, exhibits important differences in the electronic structure of the surface with respect to that of the bulk.[11–13] While only high-pressure phases of bismuth are known to become superconducting,[14] superconductivity has been reported in Bi clusters, nanowires, and bicrystals, as well as in polycrystalline forms.[15–18]

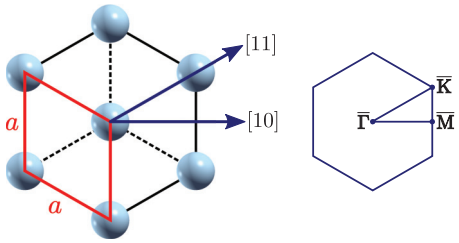

FIG. 2. (Color online) Structure of the Bi(111) top surface layer with the two distinguishable directions marked. The lattice spacing parameter is $a = 4.54$ Å (Ref. 7).

Moreover, spin-orbit coupling in bismuth, besides being more effective than in lead thus making it interesting for future applications in spintronics,[7] provides an appreciable contribution to the electron-phonon coupling.[19,20] All that considered, a detailed understanding of He bound-state energies and resonances appears to be a necessary step for a complete HAS spectroscopy of surface phonons in Bi(111).

II. Bi(111) SURFACE STRUCTURE

The (111) surface is the most important one of rhombohedral bismuth, since it is its natural cleavage plane, thus cheap and easily available. The top layer of Bi(111) displays a hexagonal structure with an atomic spacing of $a = 4.54$ Å; Fig. 2.

The electronic properties of the Bi(111) surface have been thoroughly investigated.[7,13,21] The most interesting results, reported by Ast *et al.*,[12] concern the electron and hole pockets of surface states around certain points of the SBZ. Especially the electron pockets at the six $\bar{M}$ points are expected to contribute to the surface corrugation of the electron density. It should be remembered that the presence of Fermi-surface electronic states in all directions yields a flat surface density, as observed, e.g., in Cu(111). Recently Mayrhofer *et al.*[3] have indeed reported, by means of HAS measurements, an unexpectedly large electron-density corrugation of the Bi(111) surface, in good agreement with *ab initio* calculations.

III. ATOM-SURFACE INTERACTION POTENTIAL

The potential between a He atom and a solid surface essentially consists of a short-range repulsive part originating from the Pauli repulsion between the helium closed shell and the electrons of the surface, and of a longer range attractive part due to dispersion (van der Waals) forces. A good description of the atom-surface potential including only dipole-dipole dispersion forces in the attractive part is the 3-9 potential,[22]

$$V(z) = \frac{\sqrt{27}}{2} D\left[\left(\frac{\sigma}{z}\right)^9 - \left(\frac{\sigma}{z}\right)^3\right], \qquad (1)$$

where D denotes the well depth, σ is the distance at which the potential vanishes, and $z = 3^{1/6}\sigma$ is the position of the potential minimum. The 3-9 potential, Eq. (1), is readily obtained by summing over the entire semi-infinite lattice of the individual He-solid atomic 12-6 (Lennard-Jones) potentials.[22] The eigenvalue spectrum of this potential for the motion component normal to the surface can be calculated using the

distorted wave Born approximation,[22] and is found to be

$$E_n = -D\left[1 - \frac{\pi\hbar}{3.07}\frac{n+\frac{1}{2}}{\sigma\sqrt{2mD}}\right]^6 \quad (2)$$

with m the He atom mass and E_n the nth bound-state energy. As seen in the next section, this expression for the bound states works well also in the analysis of the bound-state resonances of a semimetal surface such as Bi(111).

IV. SELECTIVE ADSORPTION RESONANCES

The kinematics of a selective adsorption resonance, where a He atom enters elastically a bound state of energy $-|E_n|$ before being scattered inelastically into the final state, is defined by the simultaneous conservation of energy and parallel momentum. The two conservation laws yield the selective-adsorption condition, expressed by the equation[23]

$$\mathbf{k_i}^2 = (\mathbf{k_i}\sin\theta_i + G_\parallel)^2 + G_\perp^2 - \frac{2m}{\hbar^2}|E_n|\,, \quad (3)$$

where $\mathbf{k_i}$ is the atom incident wave vector, θ_i is the incident angle, and $\mathbf{G} = (G_\parallel, G_\perp)$ is the surface reciprocal-lattice vector mediating the adsorption process. Here $\mathbf{G}$ is split into the components $G_\parallel$ and $G_\perp$ parallel and normal to the incidence plane, respectively.

The resonance condition, Eq. (3), can be matched either by varying the incident angle θ_i at fixed incident momentum $\mathbf{k_i}$ or by varying the incident momentum at fixed incident angle (Fig. 3).

The intensity of a bound-state resonance supported by the exchange of a reciprocal-lattice vector $\mathbf{G}$ is proportional to the squared $\mathbf{G}$th Fourier component of the surface potential at the scattering turning point. Thus bound-state resonances are only observed on a corrugated surface, as is the case for Bi(111).

For all the observable resonance features between elastic peaks a phonon must be involved. In this process, two differing channels can be distinguished, namely "incident-state" or "final-state" resonances, depending on when the helium atom is in resonance with the involved bound-state level. In the first case the helium atom enters the bound state elastically, while leaving the surface interacting with a phonon. This process yields observable changes in the elastic spectrum between the elastic scattering peaks as observed in the elastic spectra in Bi(111). In the case of "final-state" inelastic resonances, the helium atom enters the bound-state channel using the interaction with a phonon. When this helium atom leaves the surface elastically, its energy differs from the beam by the energy of the involved phonon—producing an observable feature in time-of-flight (TOF) measurements.[24] The resonance condition for the latter can be expressed by

$$\mathbf{k_i}^2 - \frac{2m}{\hbar}\omega_{\mathbf{Q}v} = (\mathbf{k_i}\sin\theta_i + G_\parallel + \mathbf{Q})^2 + G_\perp^2 - \frac{2m}{\hbar^2}|E_n| \quad (4)$$

with $\mathbf{Q}$ and $\hbar\omega_{\mathbf{Q}v}$ the wave vector and the energy of the involved phonon.

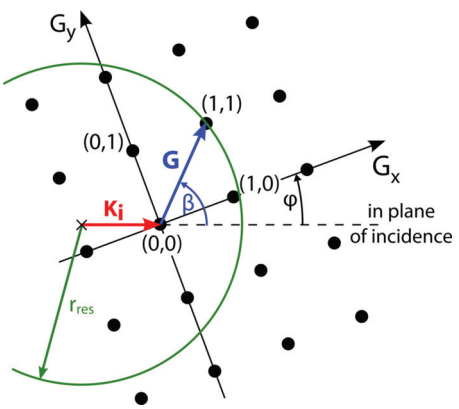

FIG. 3. (Color online) Geometrical representation of the resonance condition in Eq. (3) in the reciprocal space (for a cubic lattice). The resultant vector $\mathbf{K_i} + \mathbf{G}$ that leads to a resonant transition lies on a circle with the radius $r_{\rm res}^2 = \mathbf{k_i}^2 + \frac{2m}{\hbar^2}|E_n|$.

A. Bound-state energies and He-Bi(111) potential

In the absence of corrugation the total energy of an atom trapped in the nth bound state would be that of an atom freely moving along the surface with momentum $\hbar\mathbf{K}$ shifted by the bound-state energy $-|E_n|$, i.e.,

$$E_{\rm kin}(\mathbf{K},n) = \frac{\hbar^2 K^2}{2m} - |E_n|. \quad (5)$$

Corrugation introduces periodic components in the surface potential. The atom wave functions are Bloch states, with the appearance of gaps in the bound-state dispersion relations and mass renormalization, the latter effects being more pronounced for more deeply bound states, i.e., for atoms moving closer to the surface.[25]

In general these effects are sufficiently small and hard to detect with the present data and the available angular and energy resolution. Thus no mass renormalization is applied in the following analysis, and only the $\mathbf{G} = 0$ component of the surface potential (the laterally averaged potential) is extracted from the fitting of bound-state energies.[26]

The present measurements were performed on a HAS apparatus with a 91.5° source-target-detector geometry. The apparatus has been described in greater detail in a previous paper.[27] The time-dependent measurements in Figs. 1, 7, and 8 are plotted in two separate lines. In order to compensate for the nonlinearity of the energy scale the intensity of the measured spectrum must be multiplied by the corresponding Jacobian determinant. However, this scaling also increases the height of experimental noise on the creation side, making it difficult to distinguish peaks from noise in the creation region with large energy loss. Therefore, the energy axis of the signal was divided in equally sized energy bins. All the data points falling into one bin have been averaged in order to smooth the signal, resulting in the black line. The Bi(111) single crystal used in this study was a disk with a diameter of 15 mm which has been cleaned by Ar^+ sputtering (1.5 kV, 2 μA) and annealed in three intervals at 423 K for 6 h each prior to the measurements. The sample temperature was measured using a chromel-alumel thermocouple. First indications for surface resonance features were observed in HAS angular distributions on Bi(111) whereas the angle of incidence θ_i was changed at constant incident beam energy E_i of 15.1 meV. This allows

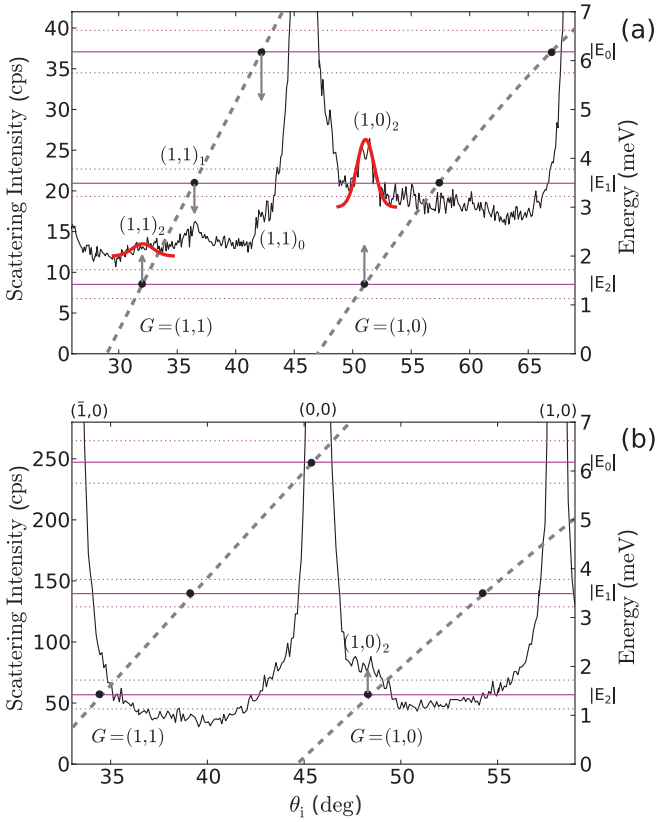

FIG. 4. (Color online) (a) Angular distribution of He atom scattering intensity (left-hand ordinate scale) from Bi(111) along a $\overline{\Gamma K}$ surface direction for a 91.5° scattering geometry at a beam energy of 15.1 meV. Besides the specular (0,0) and the two closest diffraction peaks (1,1) and (−1,−1), the angular distribution shows additional features corresponding to selective adsorption processes. The bound-state energies which would give a feature in the angular distribution are plotted (broken lines) as functions of the incident angle for the two smallest **G** vectors indexed by (1,1) and (1,0), respectively, allowing for in-plane and out-of-plane resonances (corresponding energy scale on the right-hand side). The vertical arrows associate the resonant features with the energies of three bound states. (b) Same as (a) for the $\overline{\Gamma M}$ direction.

us to extract, in a single angular distribution, information on both the surface structure (via diffraction amplitudes) and bound-state energies (via selective adsorption features, which can be either peaks or dips, depending on the phase shift between direct and resonant channels).

Figure 4(a) displays the enlarged signal of an angular distribution from Bi(111) as a function of the incident angle θ_i along a $\overline{\Gamma K}$ direction, for the crystal held at room temperature. The features observed at $\theta_i = 32°$, 37°, 42°, and 51° in the regions between the specular (0,0) and the first diffraction peaks (1,1) and (−1,−1) at $\theta_i = 45.75°$, 68.75°, and 24.75°, respectively, are attributed to selective adsorption. The analysis based on Eq. (3) allows us to assign these four resonances to bound states. This is easily done by superimposing to the angular distribution of Fig. 4(a) the curves representing the bound-state energy given by Eq. (3) as a function of θ_i for different **G** vectors, the actual values of the latter (in $Å^{-1}$) being known from the positions of the diffraction peaks. The two broken lines plotted in Fig. 4(a) correspond to the smallest **G** vectors indexed by (1,1) and (1,0). The three resonances below the specular peak are clearly associated with the (1,1) channel (in-plane resonances) and three bound states, whereas the large resonance at 51° can be associated with the (1,0) channel (out-of-plane resonance) and the same bound state as the 32° resonance. The (1,0)-channel features associated with the other two deeper bound states are expected at 58° and 66°, and are observed to correspond to a broad bump and a small peak, respectively, both hardly detectable above the background noise (no extra position mark in Fig. 4). The binding energies derived from these resonances are

$$\begin{aligned} E_0 &= (6.18 \pm 0.55)\ \text{meV}, \\ E_1 &= (3.49 \pm 0.28)\ \text{meV}, \\ E_2 &= (1.42 \pm 0.30)\ \text{meV}. \end{aligned} \tag{6}$$

Once these energy values are derived from the most prominent resonances, other weaker features can eventually be assigned to other combinations $(\mathbf{G})_n$, as for example $(1,1)_2$ and $(1,0)_1$ along the $\overline{\Gamma M}$ direction [Fig. 4(b)].

In this measurement only one strong resonance feature appears right next to the specular peak. This peak can be identified as the $(1,0)_2$ resonance.

With the experimentally determined bound-state energies the interaction potential parameters can be derived by a least-squares fit of the eigenvalue spectrum of a 3-9 potential [Eq. (2)]. The resulting parameters are

$$\begin{aligned} D &= (8.32 \pm 0.73)\ \text{meV}, \\ \sigma &= (0.297 \pm 0.012)\ \text{nm}. \end{aligned} \tag{7}$$

Figure 5 displays the 3-9 potential according to the best-fit parameters, together with its three bound states and the respective confidence intervals. The calculated potential well depth D is consistent with known values for noble-metal vicinal (corrugated) surfaces such as Cu(117) (D = 7.41 meV)(Ref. 28) and Ag(111) (D = 9.3 meV).[29]

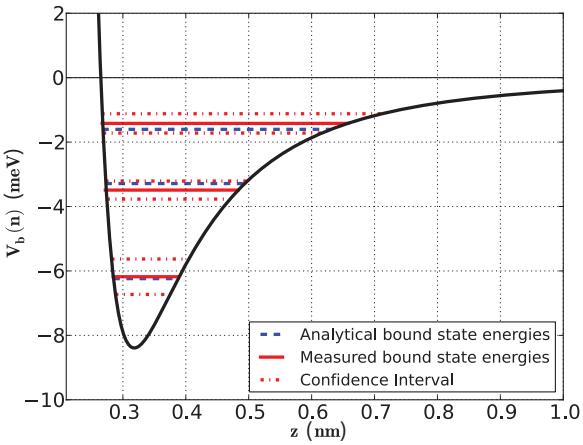

FIG. 5. (Color online) Best-fit 3-9 potential [Eq. (1)] for the He-Bi(111) atom-surface interaction with D = 8.32 meV and σ = 0.297 nm. The red (full) lines indicate the experimentally determined bound-state energies and their uncertainties (dash-dotted), the blue lines (dashed) correspond to the analytical bound-state values from Eq. (2).

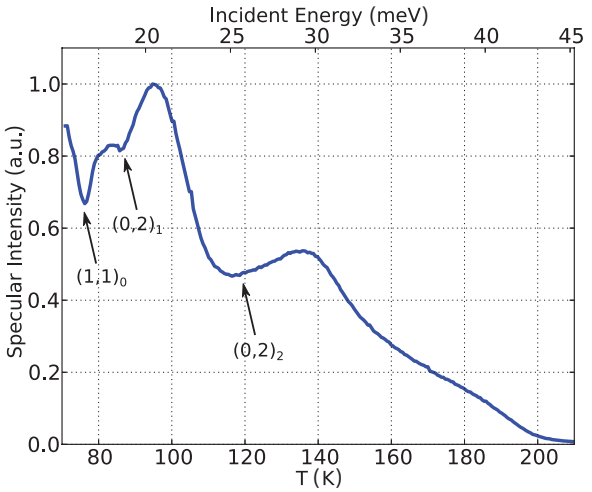

FIG. 6. (Color online) Peak height of the specularly reflected helium beam vs the nozzle temperature in the $\overline{\Gamma M}$ scattering plane. The dips at 76 and 86 K and the broad feature at 116 K can be explained with the aid of bound-state resonances.

B. Resonance effects in the specular intensity

After the determination of the bound-state energies, it is interesting to analyze the resonant features which are expected to occur in the specular intensity when measured as a function of the incident momentum. By solving Eq. (3) with respect to k_i for the specular θ_i and for given $\mathbf{G}$ and $|\epsilon_n|$, one obtains the values of k_i at which resonances are expected to occur. In principle this experiment can be made at any given incident θ_i, but fixing the incident angle at the specular peak provides the best signal-to-noise ratio.

The peak height of the specular peak was recorded while the nozzle temperature was varied between 60 and 200 K ($4.5 < k_i < 9$ Å^{-1}) (Fig. 6). Since the intensity of the incident helium beam depends on the nozzle temperature as $T_N^{-1/2}$ when resonance effects are not considered[30] and the sample is held at a constant temperature, the specular intensity should show a similar behavior. On the contrary, besides the expected continuous decrease of the intensity, some clear and intense dips at 76 and 86 and a broad feature at 116 K are recognizable in the experimental specular intensity plotted in Fig. 6. According to the predictions of Table I, the observed dips can be associated to the $(1,1)_0$, the $(0,2)_1$, and the $(0,2)_2$ resonances.

TABLE I. Expected source temperatures T_N and corresponding incident energy E_i at which bound-state resonances are expected to produce a dip in the specular peak intensity with the sample rotated to the $\overline{\Gamma M}$ direction. Resonances are labeled by $(\mathbf{G})_n$.

Resonance	T_N (K)	E_i (meV)
$(0,2)_0$	33	7.7
$(1,1)_0$	70	15.7
$(0,2)_1$	83	18.5
$(0,2)_2$	114	24.6
$(1,1)_1$	127	28.2
$(1,1)_2$	163	35.3

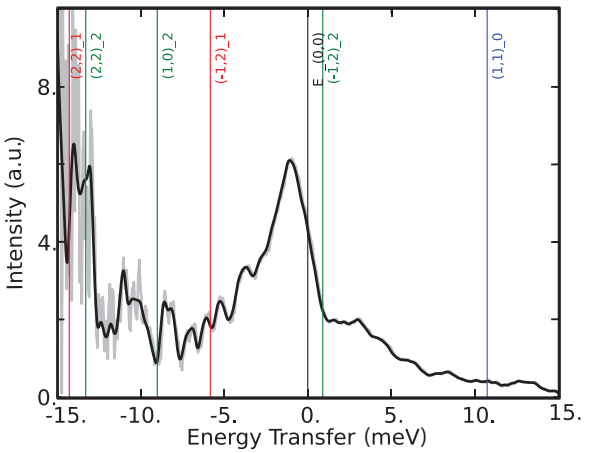

FIG. 7. (Color online) Time-of-flight (TOF) measurement of the Bi(111) surface in $\overline{\Gamma K}$ direction for $\theta_i = 44.75°$ and an incident energy of 17.79 meV. Both resonant enhancements associated with the strong $(1,0)_2$ resonance of the one-phonon peak associated with the SV3 optical mode at about -13 meV and of the multiphonon background in the one-phonon gap at about -8 meV are distinctly observed.

V. RESONANCE-ENHANCED INELASTIC SCATTERING

Once the bound-state energies have been determined with sufficient precision the positions of inelastic resonances for each bound state and each G vector involved can be calculated from Eq. (4) on the energy-transfer scale for each TOF spectrum, the phonon energy $\hbar\omega_{\mathbf{Q}\nu}$ and wave vector $\mathbf{Q}$ being related by the energy and parallel momentum conservation laws (*scan curves*). Figure 7 shows an example of a TOF spectrum represented on the energy-transfer scale taken along the $\overline{\Gamma K}$ direction for $\theta_i = 44.75°$, a scattering angle of 91.5°, an incident energy of 17.79 meV, and a surface temperature of 104 K. Besides the diffused elastic peak at $\Delta E = 0$, the positions of the expected inelastic resonances are indicated on both the positive and negative energy-transfer sides. The region where the phonon gap is expected [7.5–9.0 meV (Refs. 4 and 5)] is actually filled by a multiphonon background, as expected for the surface temperature of this experiment. This background is however strongly enhanced around -8 meV by a peak which can be assigned to the strong $(1,0)_2$ inelastic resonance whereupon the small difference between the peak and resonance positions with an adjacent dip points to a possible Fano-like character of this resonance. The effect of the other resonances are more difficult to assess as they fall into regions where important and comparatively sharp one-phonon features are expected. This can only be done through a sequence of small changes of either the incident angle or energy so as to detect a rapid intensity increase (or decrease) of a given phonon peak. Nevertheless the sharp peak at ≈13 meV, corresponding to an optical SV3 mode, is to be considered as resonance enhanced, since no such intensity would be expected for a second bilayer (third layer) optical mode.

An analysis of the resonance enhancement effect based on a sequence of slightly different incident angles and a fixed incident energy is shown in Fig. 8 for the optical-phonon region. Ten spectra for θ_i varying from 51.35° to 55.85° along

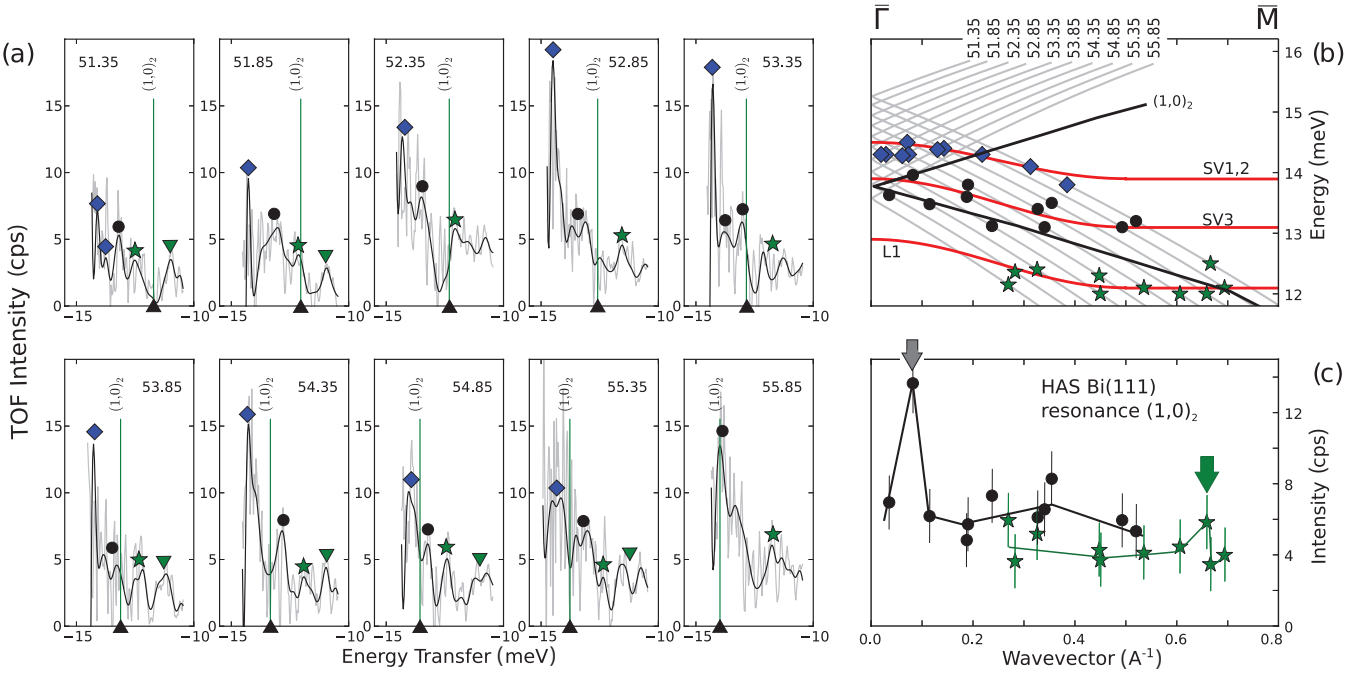

FIG. 8. (Color online) Resonant enhancement of the optical SV3 and L1 modes. (a): Ten slices from the time-of-flight measurements indicated by the dotted scan curves in (b). Diamond, circle, star, and inverted triangles indicate the measured positions of possible phonons. The black triangle indicates the position of the $(1,0)_2$ final-state inelastic resonance. The downward triangle modes correspond to the flat optical L3 branch at 11.3 meV (Ref. 4). (b) Measured phonon positions with the respective scan curves and the position of the $(1,0)_2$ resonance for the given experimental conditions. (c) Total intensities of all the measured points that were considered to correspond to the SV3 or the L1 mode, plotted as functions of the corresponding parallel wave vectors. The largest $(1,0)_2$ resonance enhancements are marked by arrows.

the $\overline{\Gamma M}$ direction are shown in Fig. 8(a) with indication of the main surface phonon peaks and of the position of the $(1,0)_2$ resonance for the $n = 2$ bound state and $\mathbf{G} = (1,0)$. The resonance condition, Eq. (4), is represented by a broken line in Fig. 8(b), superimposed to the set of scan curves for the ten incident angles. Note that the curves have all been folded into the first SBZ, so that the significant intersections are only those where the resonance and scan curves have concordant slopes. The positions of the phonons labeled in Fig. 8(a) are indicated on the corresponding scan curves with the same symbols. The comparison with the dispersion curves of the SV1, SV3, and L1 branches calculated with DFPT without spin-orbit coupling (SOC)[4,5] shows that the theoretical branches should be somewhat softer at small wave vectors for a better agreement with experiment. This softening is expected when SOC is included; actually a larger softening is found for DFPT calculations with SOC included[19,20] for free-standing slabs up to five bilayers thick. It is however difficult to infer from ultrathin free-standing slab calculations the precise phonon energies for the semi-infinite crystal. Considering the nontrivial aspects of *ab initio* calculations for the 6*sp* metals and the neglecting of van der Waals interaction, both the above calculations are to be considered in satisfactory agreement with experiment, while confirming the softening effect of SOC.

By considering now the resonance condition curve, it appears that the experimental points which fall atop or close to it have the largest intensity as appears from the plots of Fig. 8(c). In practice the theoretical SV3 branch, once it is slightly softened so as to best fit the corresponding set of experimental points, would run very close to the resonance curve along a good portion of the SBZ and would therefore benefit from the resonance enhancement. As anticipated in the Introduction, the situation of tangency between a phonon dispersion curve and a resonance curve corresponds to the surfing condition, in which the atom trapped in the bound states and the phonon created in the phonon-assisted selective adsorption process run together with the same group velocity,[10] which ensures a strong enhancement of the iHAS intensity.

In principle, the surfing conditions can be met by tuning the energy and angle of the incident He beam, provided one has a preliminary qualitative knowledge on the expected position of the phonon dispersion curves.

VI. CONCLUSION

The growing interest in the surface properties of semimetals, especially those which exhibit a topological insulator behavior, and the recent demonstration that inelastic He atom scattering from conducting surfaces can provide direct information on mode-selected electron-phonon coupling have motivated the present investigation on the He-Bi(111) interaction potential by means of helium atom scattering. The surface corrugation of the Bi(111) surface, not expected for metal surfaces but well justified for semimetals due to the existence of surface electron pocket states at the Fermi level, allowed for the observation of bound-state resonances and the corresponding surface potential profile. Three bound-state levels have been identified with binding energies of 6.18, 3.49, and 1.42 meV. For a corrugated surface the knowledge of bound-state energies is a necessary ingredient

for a detailed study of the surface phonon dispersion curves and the corresponding electron-phonon coupling strengths (mode λs). On one side the inelastic HAS amplitudes providing the mode λs should not be altered by undesired bound-state resonances. On the other side bound-state resonances can be tuned in order to enhance the inelastic HAS intensities from the optical surface modes, which are normally weak. The optical surface phonon modes in a related topological insulator like Bi_2Se_3 have been recently investigated by HAS and shown to have conspicuous anomalies attributed to the electron-phonon interaction with the Dirac-cone fermions.[31,32] A quantitative interpretation of these data requires however a careful assessment of the He-surface potential along the lines indicated in the present HAS study of the Bi(111) surface.

The profile of the atom-surface potential in the direction normal to the surface as determined from the energies of bound states, and specifically the potential depth D, together with the knowledge of the surface corrugation provide a complete picture of the interaction potential,[26] which is useful information in a variety of other applications. We note, for example, that corrugated conducting surfaces like those of semimetals allow for the selective adsorption, either elastic or inelastic, also of chemical species more interesting than the inert He atoms. In general, the selective adsorption of gas species into a surface bound state can provide a precursor state for surface reactions and may have paramount importance in the characterization of heterogeneous catalysis.

ACKNOWLEDGMENTS

Financial support was provided by the ERDF Program of the European Union, the Region of Styria and the Federation of Carinthian Industries. One of us (G.B.) acknowledges the Ikerbasque Foundation (project ABSIDES) for support.

*patrick.kraus@tugraz.at

[1] I. Y. Sklyadneva, G. Benedek, E. V. Chulkov, P. M. Echenique, R. Heid, K.-P. Bohnen, and J. P. Toennies, Phys. Rev. Lett. **107**, 095502 (2011).
[2] G. Benedek, M. Bernasconi, V. Chis, E. Chulkov, P. Echenique, B. Hellsing, and J. Toennies, J. Phys.: Condens. Matter **22**, 084020 (2010).
[3] M. Mayrhofer-Reinhartshuber, A. Tamtögl, P. Kraus, K. H. Rieder, and W. E. Ernst, J. Phys.: Condens. Matter **24**, 104008 (2012).
[4] A. Tamtögl, P. Kraus, M. Mayrhofer-Reinhartshuber, D. Campi, M. Bernasconi, G. Benedek, and W. E. Ernst, Phys. Rev. B **87**, 035410 (2013).
[5] A. Tamtögl, P. Kraus, M. Mayrhofer-Reinhartshuber, D. Campi, M. Bernasconi, G. Benedek, and W. E. Ernst, Phys. Rev. B **87**, 159906(E) (2013).
[6] J. Braun, P. Ruggerone, G. Zhang, J. P. Toennies, and G. Benedek, Phys. Rev. B **79**, 205423 (2009).
[7] P. Hofmann, Prog. Surf. Sci. **81**, 191 (2006).
[8] D. Evans, V. Celli, G. Benedek, J. P. Toennies, and R. B. Doak, Phys. Rev. Lett. **50**, 1854 (1983).
[9] G. Bracco, M. D'Avanzo, C. Salvo, R. Tatarek, S. Terreni, and F. Tommasini, Surf. Sci. **189**, 684 (1987).
[10] G. Benedek, P. Echenique, J. Toennies, and F. Traeger, J. Phys.: Condens. Matter **22**, 304016 (2010).
[11] K. Behnia, Science **321**, 497 (2008).
[12] C. R. Ast and H. Höchst, Phys. Rev. Lett. **87**, 177602 (2001).
[13] M. Hengsberger, P. Segovia, M. Garnier, D. Purdie, and Y. Baer, Eur. Phys. J. B **17**, 603 (2000).
[14] J. Wittig, Z. Phys. **195**, 215 (1966).
[15] B. Weitzel and H. Micklitz, Phys. Rev. Lett. **66**, 385 (1991).
[16] C. Vossloh, M. Holdenried, and H. Micklitz, Phys. Rev. B **58**, 12422 (1998).
[17] M. Tian, N. Kumar, M. H. W. Chan, and T. E. Mallouk, Phys. Rev. B **78**, 045417 (2008).
[18] L. A. Baring, R. R. da Silva, and Y. Kopelevich, J. Low Temp. Phys. **37**, 889 (2011).
[19] V. Chis, G. Benedek, P. M. Echenique, and E. V. Chulkov, Phys. Rev. B **87**, 075412 (2013).
[20] G. Huang and J. Yang, J. Phys.: Condens. Matter **25**, 175004 (2013).
[21] C. R. Ast and H. Höchst, Phys. Rev. B **67**, 113102 (2003).
[22] M. W. Cole and T. T. Tsong, Surf. Sci. **69**, 325 (1977).
[23] H. Hoinkes and H. Wilsch, *Helium Atom Scattering from Surfaces* (Springer-Verlag, Berlin, 1992), Chap. 7, pp. 113–173.
[24] G. Brusdeylins, R. Doak, and J. Toennies, J. Chem. Phys. **75**, 1784 (1981).
[25] V. Celli, N. Garcia, and J. Hutchison, Surf. Sci. **87**, 112 (1979).
[26] H. Hoinkes, Rev. Mod. Phys. **52**, 933 (1980).
[27] A. Tamtögl, M. Mayrhofer-Reinhartshuber, N. Balak, W. E. Ernst, and K. H. Rieder, J. Phys.-Cond. Mat. **22**, 304019 (2010).
[28] J. Lapujoulade, Y. Lejay, and N. Papanicolaou, Surf. Sci. **90**, 133 (1979).
[29] J. M. Horne, S. C. Yerkes, and D. R. Miller, Surf. Sci. **93**, 47 (1980).
[30] D. R. Miller, *Atomic and Molecular Beam Methods* (Oxford University Press, New York, Oxford, 1988), Chap. 2, pp. 14–53.
[31] X. Zhu, L. Santos, R. Sankar, S. Chikara, C. Howard, F. C. Chou, C. Chamon, and M. El-Batanouny, Phys. Rev. Lett. **107**, 186102 (2011).
[32] X. Zhu, L. Santos, C. Howard, R. Sankar, F. C. Chou, C. Chamon, and M. El-Batanouny, Phys. Rev. Lett. **108**, 185501 (2012).